

Bayesian Learning of Chemisorption for Bridging Complexities of Electronic Descriptors

Siwen Wang

Virginia Tech

Hemanth Pillai

Virginia Tech

Hongliang Xin (✉ hxin@vt.edu)

Virginia Tech <https://orcid.org/0000-0001-9344-1697>

Article

Keywords: d-band reactivity theory, Bayesian learning, bridging complexities, surface chemistry, catalysis

Posted Date: July 30th, 2020

DOI: <https://doi.org/10.21203/rs.3.rs-48646/v1>

License:  This work is licensed under a Creative Commons Attribution 4.0 International License.

[Read Full License](#)

Version of Record: A version of this preprint was published at Nature Communications on November 30th, 2020. See the published version at <https://doi.org/10.1038/s41467-020-19524-z>.

1 **Bayesian Learning of Chemisorption for Bridging Complexities of**
2 **Electronic Descriptors**

3 Siwen Wang[†], Hemanth Somarajan Pillai[†], and Hongliang Xin^{*}

4 *Department of Chemical Engineering,*

5 *Virginia Polytechnic Institute and State University, Blacksburg, VA 24061, USA*

6 **Abstract**

7 Building upon the *d*-band reactivity theory in surface chemistry and catalysis, we develop a Bayesian
8 learning approach to probing chemisorption processes at atomically tailored metal sites. With representative
9 species, e.g., *O and *OH, the Bayesian model trained with *ab initio* adsorption properties of transition
10 metals predicts site reactivity at a diverse range of intermetallics and near-surface alloys while naturally
11 providing uncertainty quantification from posterior sampling. More importantly, this conceptual framework
12 sheds light on the orbitalwise nature of chemical bonding at adsorption sites with *d*-states characteristics
13 ranging from bulk-like semi-elliptic bands to free-atom-like discrete energy levels, bridging complexities
14 of electronic descriptors for the prediction of novel catalytic materials.

* hxin@vt.edu

15 Adsorption of molecules or their fragments at transition-metal surfaces is a fundamental pro-
16 cess for many technological applications, such as chemical sensing, molecular self-assembly, and
17 heterogeneous catalysis. Because of the convoluted interplay between electron transfer and orbital
18 coupling, chemical bonding can be formidably complex. Recent decades have brought major ad-
19 vances in spectroscopic tools [1, 2] which reveal orbitalwise information of chemisorbed systems
20 and concurrently in predicting chemical reactivity at sites of interest via electronic factors, e.g.,
21 number of valence d -electrons [3], density of d -states at the Fermi level [4], d -band center [5],
22 and d -band upper edge [6, 7]. Compared with a full quantum-mechanics treatment of many-body
23 systems, the simplicity of physics-inspired descriptors comes at a cost of limited generalization,
24 particularly for high-throughput materials screening in which variations of site composition and
25 configuration are sufficiently large to invalidate the perturbation approximation. Incorporation
26 of multi-fidelity site features into reactivity models with machine learning (ML) algorithms has
27 shown early promise for the prediction of adsorption energies with an accuracy comparable to the
28 typical error ($\sim 0.1\text{--}0.2$ eV) of density functional theory (DFT) calculations [8–12]. However,
29 the approach is largely black-box in nature, prohibiting its physical interpretation. Developing
30 a theory-based, generalizable model of chemisorption that bridges complexities of electronic de-
31 scriptors and predicts the binding affinity of active sites to key reaction intermediates with uncer-
32 tainty quantification represents one of the biggest challenges in fundamental catalysis.

33 Here we present a Bayesian inference approach to probing chemisorption processes at metal
34 sites by learning from *ab initio* datasets. The model is built upon the basic framework of the d -band
35 reactivity theory [5] while employing a Newns-Anderson-type Hamiltonian [13, 14] to capture es-
36 sential physics of adsorbate-substrate interactions. Such types of simplified Hamiltonians were
37 originally used for describing magnetic properties of impurities in a bulk metallic host [13] and
38 later extended with success by Newns and Grimley to chemisorption at surfaces [14, 15]. A basis
39 set of orbitals consisting of the adsorbate and substrate states was used for solving the hybridiza-
40 tion problem within a self-consistent Hartree-Fock scheme [14]. Despite a remarkable success in
41 advancing the basic understanding of adsorption phenomena at surfaces, particularly for d -block
42 metals [6], its application in materials design remains limited due to the lack of accurate model
43 parameters and meaningful error estimates. Bayesian inference produces the posterior probability
44 distribution of model parameters under the influence of observations and prior knowledge [16].
45 With representative species, e.g., $^*\text{O}$ and $^*\text{OH}$, we demonstrate the predictive performance and
46 physical interpretability of the Bayesian models for chemical bonding at a diverse range of in-

47 termetallics and near-surface alloys, bridging complexities of electronic descriptors in search of
 48 novel catalytic materials.

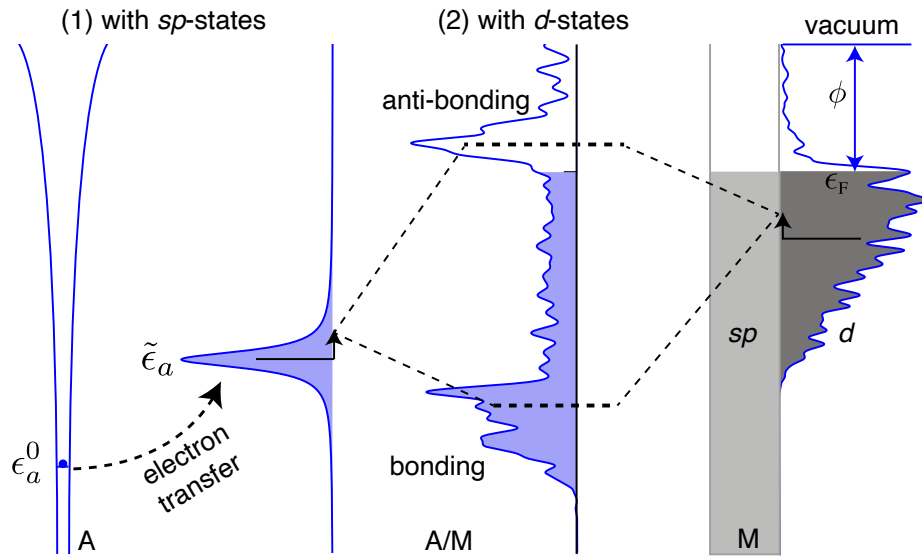


Figure 1. Illustration of chemical bonding at transition-metal surfaces within the *d*-band reactivity theory. An adsorbate A with a valence electron at a discrete energy level ϵ_a^0 first interacts with the free-electron-like *sp*-states of the substrate M, forming a broadened resonance at $\tilde{\epsilon}_a$ accompanied with electron transfer. Conceptually, it further overlaps and hybridizes with the narrowly distributed *d*-states, which leads to a splitting into bonding and anti-bonding states. The work function ϕ and Fermi level ϵ_F of M are marked.

49 Results

50 **The *d*-band reactivity theory.** Within the basic framework of the *d*-band reactivity theory for
 51 transition-metal surfaces, the formation of the adsorbate-metal bond conceptually takes place in
 52 two consecutive steps [5]. First, the adsorbate orbital (or orbitals) $|a\rangle$ at ϵ_a^0 couples to the delocalized,
 53 free-electron-like *sp*-states of the metal substrate, leading to a Lorenzian-shaped resonance
 54 state at $\tilde{\epsilon}_a$. Second, the adsorbate resonance state interacts with the localized, narrowly-distributed
 55 metal *d*-states, shifting up in energies due to the orthogonalization penalty for satisfying the Pauli
 56 principle and then splitting into bonding and anti-bonding states. The first step interaction con-
 57 tributes a constant ΔE_0 albeit the largest part of chemical bonding. The variation in adsorption
 58 energies from one metal to another is determined by the metal *d*-states. This part of the interaction
 59 energy ΔE_d can be further partitioned into orbital orthogonalization and hybridization contribu-
 60 tions [17]. As a first-order approximation, the orbital hybridization energy can be evaluated by
 61 the changes of integrated one-electron energies [18]. The orbital orthogonalization cost is con-

sidered simply as proportional to the product of interatomic coupling matrix and overlap matrix, VS , or equivalently αV_{ad}^2 , where V_{ad}^2 is the interatomic coupling matrix element squared when the interacting atoms are aligned along z -axis and α is the orbital overlap coefficient. The absolute value of V_{ad}^2 can be written as $\beta \bar{V}_{ad}^2$, in which the standard values of \bar{V}_{ad}^2 relative to Cu are readily available on the Solid State Table [19]. The overall adsorption energy ΔE can then be written as the sum of the energy contributions from the sp -states ΔE_0 and the d -states ΔE_d , with the latter of which depending on the symmetry and degeneracy of the adsorbate valence orbitals. Another important information from this framework is the evolving density of states projected onto the adsorbate orbital(s) upon adsorption, ρ_a . A full account of the theoretical framework is presented in the Method section.

There are a number of unknown parameters within the basic framework of the d -band reactivity theory as discussed above, including the energy contribution from the sp -band ΔE_{sp}^0 , adsorbate resonance energy $\tilde{\epsilon}_a$ relative to the Fermi level, sp -band chemisorption function Δ_{sp}^0 , orbital overlap coefficient α , and orbital coupling coefficient β . By least-squares fitting of the adsorbate density of states as in Eq. 2 and the integrated one-electron energy changes to those from DFT calculations [20, 21], the Schmickler model of electron transfer has been developed to understand H_2 evolution/oxidation and OH^- adsorption at metal-electrolyte interfaces. However, the deterministic fitting of adsorption properties from a single surface is prone to overfitting or trapping into a locally optimal region, limiting its application in catalysis.

Bayesian learning. We instead employ Bayesian learning to infer the vector of model parameters $\vec{\theta} = (\Delta E_{sp}^0, \tilde{\epsilon}_a, \Delta_{sp}^0, \alpha, \beta)'$ from the evidence, i.e., *ab initio* adsorption properties, along with prior knowledge if available [16]. In Bayes' view, those parameters are not deterministic point values, but rather a probabilistic distribution reflecting not necessarily the random nature of physical variables but rather the uncertainty. The use of parameter distributions as opposed to computationally-derived point values has obvious advantages for uncertainty quantification. In the chemical sciences, Bayesian learning has been used for calibration and validation of thermodynamic models for the uptake of CO_2 in mesoporous silica-supported amines [22], designing the Bayesian error estimation functional with van der Waals correlations [23], and identifying potentially active sites and mechanisms of catalytic reactions [24], just to name a few. The Bayesian approach allows one to infer the posterior probability distribution $P(\vec{\theta}|\mathcal{D})$ for latent variables based on the prior $P(\vec{\theta})$ as well as the likelihood function $P(\mathcal{D}|\vec{\theta})$ subject to the observation \mathcal{D} . The

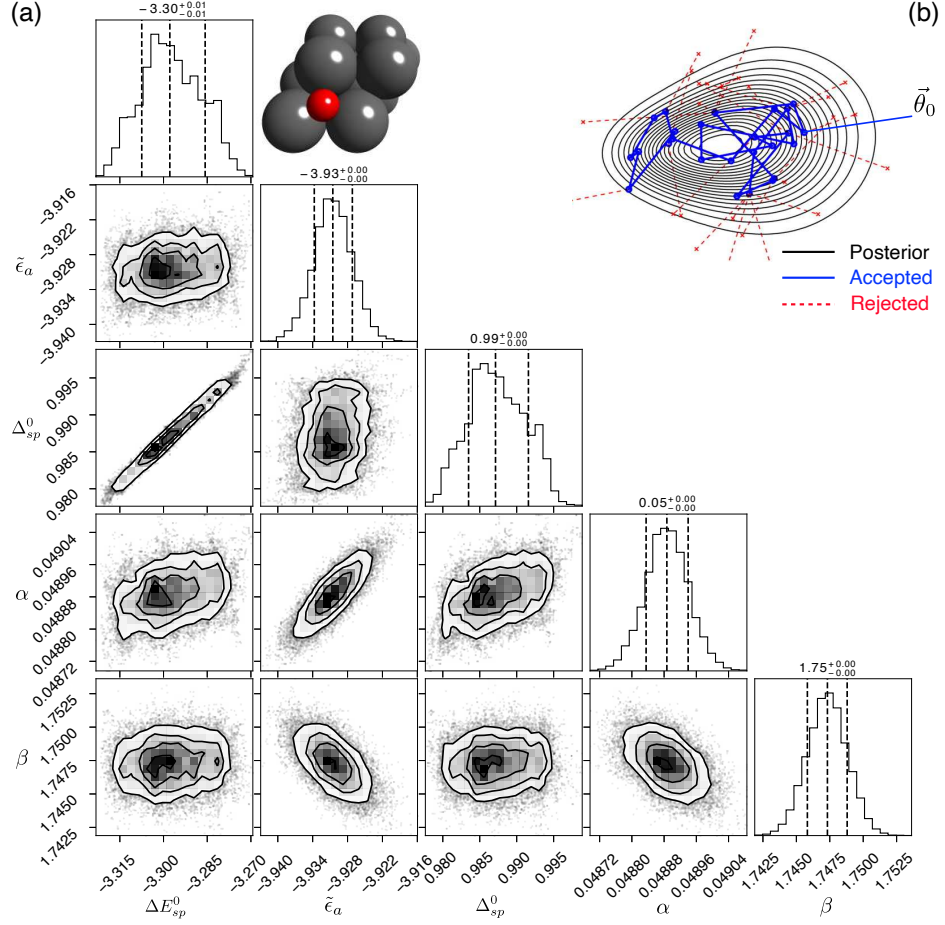


Figure 2. Bayesian parameterization. **a** The co-variance of the joint posterior distribution for each parameter pair and the 1D histogram of model parameters (ΔE_{sp}^0 , $\tilde{\epsilon}_a$, Δ_{sp}^0 , α , and β) from MCMC simulations for *O adsorption at the fcc-hollow site of the {111}-terminated transition-metal surfaces. A top view of the model structure is shown in inset. **b** Schematic illustration of the MCMC sampling in a multi-dimensional parameter space.

93 mathematical relationship between the prior, observation, and posterior is given by the Bayes' 94 theorem [16], $P(\vec{\theta}|\mathcal{D}) = P(\mathcal{D}|\vec{\theta})P(\vec{\theta})/P(\mathcal{D})$. Our initial belief about likely parameter values is 95 provided by weakly informative priors to minimize potential bias. For example, ΔE_{sp}^0 and $\tilde{\epsilon}_a$ can 96 be estimated from DFT calculations of the adsorbate on a simple metal, e.g., sodium (Na) at the 97 face-centered cubic (fcc) phase. Specifically, we took Normal for floating-point variables unre- 98 stricted in sign, LogNormal for non-negative parameters, and Uniform for others (see the details 99 of Bayesian learning and parameter choices in the Method section). Computing the normalizing 100 constant $P(\mathcal{D})$, denominator of the posterior distribution, is impossible in most practical scenar-

ios. To avoid this complication, the Markov chain Monte Carlo (MCMC) method [25], whose sampling criterion only depends on the relative posterior density of the newly explored point and its preceding point, is used. To compute the transition probability of each MCMC step, we define the sum of the (negative) logarithm of the likelihood functions corresponding to projected density of states onto each adsorbate orbital and binding energies with a hyper-parameter adjusting the weight of two contributing metrics, see details in the Method section for its optimization. After a large number of MCMC samplings, burning (discard) of the first half of the trajectory and then thinning (1 out of 5 samplings) were performed before extracting converged values from the joint posterior distributions. The convergence of the MCMC sampling is checked by using parallel chains with different starting parameter sets such that the variance of interchain samplings is close or within 1.2–1.5 times to that of intrachains [25]. The complete code of Bayesian inference is available at a Github repository <https://github.com/hlxin/bayeschem> for public access.

Model development. In Fig. 2(a), we are showing the co-variance of the joint posterior distribution for each parameter pair and the 1D histogram of model parameters (ΔE_{sp}^0 , $\tilde{\epsilon}_a$, Δ_{sp}^0 , α , and β) from MCMC simulations for *O adsorption at the fcc-hollow site of the {111}-terminated transition-metal surfaces (Cu, Ag, Au, Ni, Pd, Pt, Co, Rh, Ir, and Ru). We assume three degenerate O_{2p} orbitals as used before [26] for demonstration of the approach, while later extend it to multi-orbital models. To attain converged posterior distributions, 200k MCMC sampling steps with the Metropolis-Hastings algorithm were performed in a multi-dimensional parameter space illustrated in Fig. 2(b). In Fig. 2, the approximate contours for 68%, 95%, and 99% confidence regions are shown at the lower triangle, showing little to no correlation between most of latent-variable pairs.

With the converged Bayesian sampling, in Fig. 3(a), it shows the model-predicted adsorption energies of *O at the fcc-hollow site of transition-metal surfaces, with a mean absolute error (MAE) ~ 0.17 eV compared to DFT calculations. The standard deviation of model prediction using the posterior distribution of model parameters ($\vec{\theta}$, $\vec{\sigma}$) is overlaid, providing for the first time uncertainty quantification of adsorption energies within the *d*-band reactivity theory. Figure 3(b) shows DFT-calculated and model-constructed projected density of states onto the O_{2p} orbital using the posterior means of model parameters, taking Pt(111) as an example (see all the surfaces in Fig. S1). The chemisorption function $\Delta(\epsilon)$ and its Hilbert transform $\Lambda(\epsilon)$ along with the straight adsorbate line ($\epsilon - \tilde{\epsilon}_a$) are shown for the graphical solution of the Newns-Anderson-Grimley model [14, 15]. The intersects indicated by solid circles in Fig. 3(b) represent the O_{2p} -Pt_{5d} bonding and

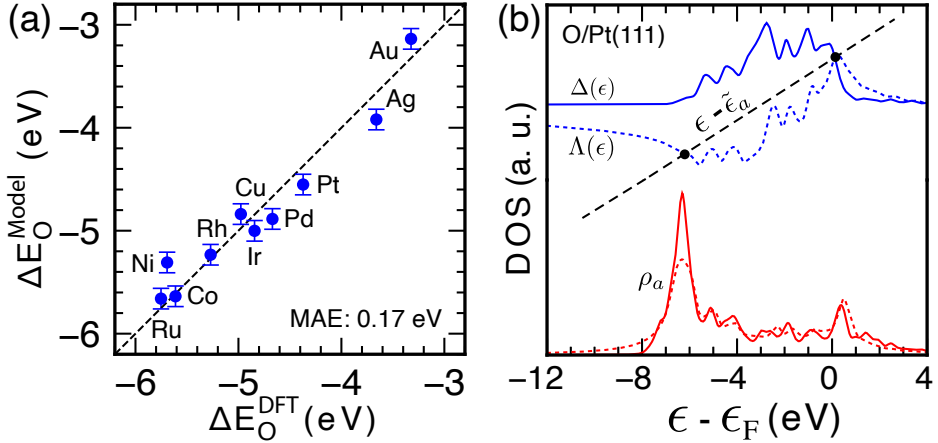


Figure 3. Model-predicted adsorption properties. **a** DFT-calculated ${}^*\text{O}$ adsorption energies (atomic O as the reference) at transition-metal surfaces vs. model prediction using the posterior distribution of model parameters ($\vec{\theta}$, $\vec{\sigma}$). Error bars represent the standard deviation of model prediction with 1000 random draws from converged trajectories. **b** Projected density of states onto the O_{2p} orbital from DFT calculations (solid) and model prediction (dashed) using the posterior means of model parameters, taking Pt(111) as an example. The graphical solution to the Newns-Anderson-Grimley model is also shown, in which the adsorbate-substrate bonding and anti-bonding states are clearly captured.

132 anti-bonding states, with the latter above the Fermi level, suggesting a strong covalent interaction
 133 of ${}^*\text{O}$ at Pt(111). Given the simplicity of the model, the clearly captured electronic structure of
 134 the adsorbate-substrate system and the reactivity trend are satisfying.

135 To demonstrate the approach for general adsorbates with multiple valence orbitals that possibly
 136 contribute to bonding, we have explicitly treated O_{2p} states with the doubly degenerate p_{xy} orbitals
 137 and the single p_z orbital in Bayesian learning. We infer model parameters ($\tilde{\epsilon}_a$, Δ_{sp}^0 , and β) cor-
 138 responding to each non-equivalent adsorbate orbital together with an orbital-independent α [27]
 139 and a global parameter ΔE_{sp}^0 . The posterior parameter distributions are shown in Fig. S2. From
 140 the posterior means of model parameters, we can see that the orbital coupling coefficient β of p_{xy}
 141 (1.67 eV^{-1}) is smaller than that of p_z (1.77 eV^{-1}), consistent with the symmetry analysis that the
 142 p_{xy} orbitals that are parallel to a surface form π -bonds with the d -states, while the p_z orbital can in-
 143 teract through a stronger σ bond. A weaker coupling manifests itself in a narrower orbital splitting
 144 of π/π^* than that of σ/σ^* , which has been previously observed using the angle-resolved photoe-
 145 mission spectroscopy on Cu and Ni [28]. In Fig. S3 and S4, it shows that the model-constructed
 146 projected density of states onto symmetry-resolved orbitals closely resemble the DFT-calculated

¹⁴⁷ distributions and the predicted values of ${}^*\text{O}$ adsorption energies have a MAE ~ 0.17 eV, suggesting
¹⁴⁸ the robustness and generalizability of the approach.

¹⁴⁹ To test prediction capability of the Bayesian model for unseen systems, we took the ${}^*\text{OH}$
¹⁵⁰ species as a case study because of its fundamental importance in understanding the nature of
¹⁵¹ chemical bonding [29] and practical interests as a key reactivity descriptor in metal-catalyzed
¹⁵² electrochemical O_2 reduction [30], CO_2 reduction [31], H_2 oxidation in alkaline electrolytes [32],
¹⁵³ etc. Three frontier molecular orbitals, i.e., 3σ , 1π , and $4\sigma^*$, are assumed to be involved in chemi-
¹⁵⁴ cal bonding [29]. Symmetry-resolved, molecular orbital density of states projected onto OH along
¹⁵⁵ with adsorption energies are used as the DFT ground truth Y in Eq. 6. With the Bayesian model
¹⁵⁶ developed here (see Fig. S5-7 for posterior parameter distributions, model-predicted adsorption
¹⁵⁷ energies and projected density of states on training samples), we predict ${}^*\text{OH}$ binding energies at
¹⁵⁸ a diverse range of intermetallics and near-surface alloys. Specifically, we included A_3B , $\text{A}'@\text{A}_{\text{ML}}$,
¹⁵⁹ $\text{A}-\text{B}@\text{A}_{\text{ML}}$, $\text{A}_3\text{B}@\text{A}_{\text{ML}}$, $\text{A}@\text{A}_3\text{B}$, and $\text{A}@\text{AB}_3$, where A (A') represents 10 fcc/hcp metals used in
¹⁶⁰ the model development and B covers d -metals across the periodic table (see ref [33] for structural
¹⁶¹ details and tabulated data). The A sites of above-mentioned surfaces exhibit diverse characteristics
¹⁶² of the metal d -states ranging from bulk-like semi-elliptic bands to free-atom-like discrete energy
¹⁶³ levels [34], as illustrated in Fig. 4(a) using Pt and Ag_3Pt as examples. Similar to previous observa-
¹⁶⁴ tions of single-atom alloys with coinage metal hosts [34, 35], a reactive guest metal often exhibits
¹⁶⁵ peaky signatures within the d -band due to the energy misalignment of coupling $d-d$ orbitals [7]. A
¹⁶⁶ direct consequence of such diverse electronic properties of adsorption sites is that no single elec-
¹⁶⁷ tronic descriptor can capture the local chemical reactivity accurately. Encouragingly, the Bayesian
¹⁶⁸ model, parameterized using 10 pristine transition-metal data, predicts ${}^*\text{OH}$ adsorption energies on
¹⁶⁹ 512 alloy surfaces with a MAE 0.16 eV, see Fig. 4(b), similar to data-driven ML models [8–11]
¹⁷⁰ and outperforming the state-of-the-art electronic descriptors, e.g., the d -band center ϵ_d (MAE: 0.20
¹⁷¹ eV) and upper edge ϵ_u (MAE: 0.23 eV).

¹⁷² **Orbitalwise interpretation of chemical bonding.** More importantly, the Bayesian framework
¹⁷³ with built-in physics allows us to quantitatively interrogate the underlying mechanism of chemical
¹⁷⁴ bonding that is difficult to obtain from purely data-driven regression models. Taking ${}^*\text{OH}$ ad-
¹⁷⁵ sorption at the M (10 fcc/hcp metals) site of $\{111\}$ -terminated Ag_3M intermetallics as examples,
¹⁷⁶ Fig. 4(c) shows the partition of ${}^*\text{OH}$ adsorption energies resulting from the 2nd step interaction
¹⁷⁷ (ΔE_d) into orbital orthogonalization and hybridization. As we can see, for 3 d , 4 d , and 5 d series

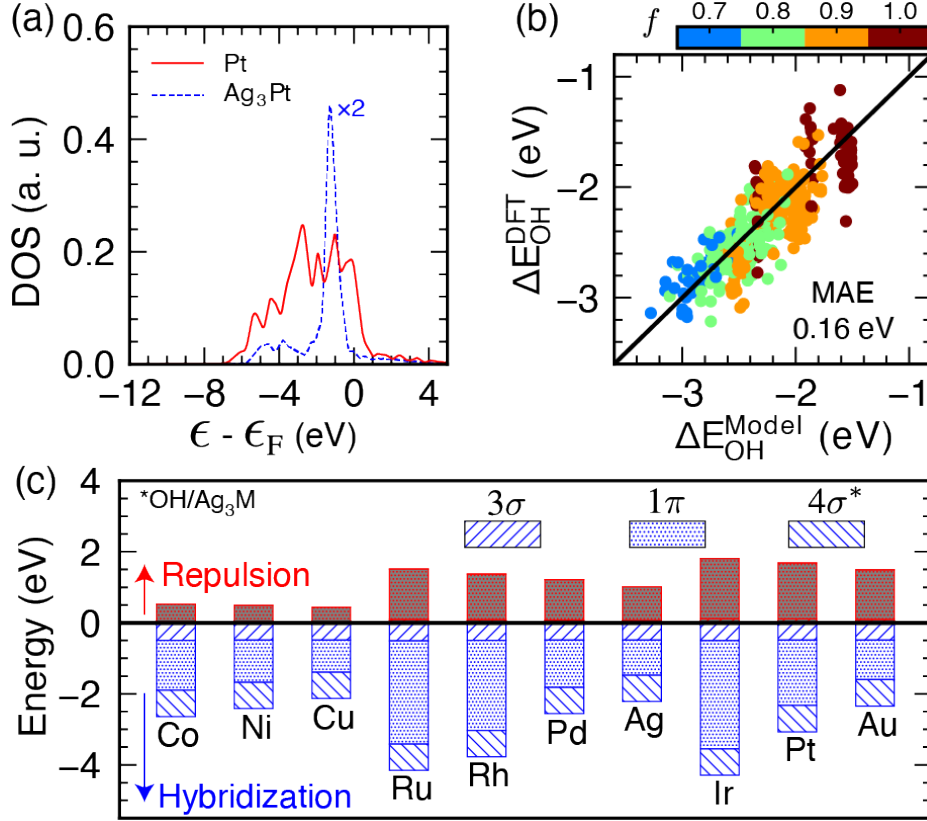


Figure 4. Model test and interpretation. **a** The d -states of a transition-metal site exhibit diverse characteristics ranging from bulk-like semi-elliptic bands to free-atom-like discrete energy levels (Pt and Ag_3Pt as examples). **b** DFT-calculated vs. model-predicted adsorption energies of ${}^*\text{OH}$ at the atop site of $\{111\}$ -terminated intermetallics and near-surface alloys. **c** Partition of ${}^*\text{OH}$ adsorption energies at the M site of Ag_3M into orbital hybridization and orthogonalization of 3σ , 1π , and $4\sigma^*$ orbitals with the metal d -states.

of the guest metal M, the orthogonalization and hybridization contributions decrease in magnitude from left to right across the periodic table, while the hybridization dominates the reactivity trends. The changes in ΔE_d^{hyb} can be understood from the Newns-Anderson-Grimley model, with the position and occupancy of adsorbate-substrate anti-bonding states tracking with the d -band center or upper edge. The orthogonalization energy is proportional to f and V_{ad}^2 (see Eq. 4), which are offsetting each other to a certain extent (V_{ad}^2 decreases while f increases across $3d$, $4d$, and $5d$ series), leading to a less dominant role than the hybridization. The orbitalwise contributions from 3σ , 1π , and $4\sigma^*$ shown in Fig. 4(c) with different fill patterns suggest that the main contribution of ${}^*\text{OH}$ adsorption at d -metal surfaces is from the 1π orbital. This is supported by projected molecular orbital density of states in Fig. S7, which shows that 3σ and $4\sigma^*$ are forming resonance

188 states after their interactions with the *sp*-states of the metal site without noticeable splitting due
189 to *d*-states. Thus, they do not contribute to the observed trend of *OH adsorption. The Bayesian-
190 optimized orbital coupling coefficients of 3σ and $4\sigma^*$ are rather small (.12 and .001 as shown in
191 Fig. S5, respectively), supporting unfavorable orbital overlaps with the *d*-states. This rationalizes
192 the observation that *OH prefers the nearly-parallel adsorption geometry on most of the *d*-metals
193 to maximize the interaction of the 1π orbital with metal *d*-states, while *OH on Na(111) adsorbs
194 more strongly in a up-straight orientation because of a lack of such directional interactions. This
195 orbitalwise insight of chemical bonding could provide guidance in tailoring orbital-specific char-
196 acteristics of the metal *d*-band for desired catalytic properties through site engineering.

197 Conclusions

198 To conclude, we present the first Bayesian model of chemisorption by learning from *ab initio*
199 adsorption properties. The model leverages the well-established *d*-band reactivity theory and a
200 Newns-Anderson-type Hamiltonian for capturing essential physics of chemisorption processes.
201 We demonstrated that the Bayesian models of descriptor species, e.g., *O and *OH, optimized
202 with pristine transition-metal data predicts adsorption energies at a diverse range of atomically-
203 tailored metal sites with a MAE \sim 0.1–0.2 eV while providing uncertainty quantification. In-
204 corporation of physics-based models into data-driven ML algorithms, e.g., deep learning, might
205 hold the promise toward developing highly accurate while interpretable reactivity models. Fur-
206 thermore, this conceptual framework can be broadly applied to unravel orbital-specific factors
207 governing adsorbate-substrate interactions, paving the path toward design strategies to go beyond
208 adsorption-energy scaling limitations in catalysis.

209 Methods

210 **DFT calculations** Spin-polarized DFT calculations were performed through Quantum ESPRESSO [36]
211 with ultrasoft pseudopotentials. The exchange-correlation was approximated within the generalized gra-
212 dient approximation (GGA) with Perdew-Burke-Ernzerhof (PBE) [37]. {111}-terminated metal surfaces
213 were modelled using (2×2) supercells with 4 layers and a vacuum of 15 Å between two images. The bot-
214 tom two layers were fixed while the top two layers and adsorbates were allowed to relax until a force criteria
215 of .1 eV/Å. A plane wave energy cutoff of 500 eV was used. A Monkhorst-Pack mesh of $6 \times 6 \times 1$ was used
216 to sample the Brillouin zone, while for molecules and radicals only the Gamma point was used. Gas phase
217 species of O and OH were used as the reference for adsorption energies of *O and *OH, respectively. The
218 projected atomic and molecular density of states were obtained by projecting the eigenvectors of the full

219 system at a denser k -point sampling ($12 \times 12 \times 1$) with a energy spacing 0.01 eV onto the ones of the part, as
 220 determined by gas-phase calculations. Further details and tabulated data can be found in ref [9].

221 **The d -band reactivity theory** To revisit the d -band theory of chemisorption along with new developments,
 222 let's consider a metal substrate M in which electrons occupy a set of continuous states with one-electron
 223 wavefunctions $|k\rangle$ and eigenenergies ϵ_k , and an isolated adsorbate species A with a valence electron de-
 224 scribed by an atomic wavefunction $|a\rangle$ at ϵ_a^0 , see Fig. 1. When the adsorbate is brought close to the sub-
 225 strate, the two sets of states will overlap and hybridize with each other. The strength of such interactions
 226 is determined by the coupling integral $V_{ak} = \langle a|\hat{\mathcal{H}}|k\rangle$, where $\hat{\mathcal{H}}$ is the system Hamiltonian. Within the
 227 Newns-Anderson-Grimley model of chemisorption [13–15], $\hat{\mathcal{H}}$ is defined as,

$$\hat{\mathcal{H}} = \sum_{\sigma} \left\{ \epsilon_{a\sigma} n_{a\sigma} + \sum_k \epsilon_k n_{k\sigma} + \sum_k (V_{ak} c_{k\sigma}^{\dagger} c_{a\sigma} + H.c.) \right\}, \quad (1)$$

228 where σ denotes the electron spin, n is the orbital occupancy operator, and c^{\dagger} and c represent the creation
 229 and annihilation operator, respectively. The first two terms in Eq. 1 are the one-electron energies from
 230 the adsorbate and the substrate when they are infinitely separated in space. The last term captures the
 231 coupling, or intuitively electron hopping, between the adsorbate orbital $|a\rangle$ and a continuum of substrate
 232 states $|k\rangle$. If the one-electron states of the whole system can be described as a linear combination of the
 233 unperturbed adsorbate and substrate states, the one-electron Schrödinger equation can be solved using the
 234 Green's function approach [14]. In Fig. 1, we illustrate the chemisorption process of a simple adsorbate onto
 235 a d -block metal site characterized by delocalized sp -states and localized d -states [17]. The interaction of the
 236 adsorbate state at ϵ_a^0 with the structureless sp -states, typically accompanied with electron transfer from/to
 237 the Fermi sea, results in a broadened resonance (or so-called renormalized adsorbate state) at a perturbed
 238 energy level $\tilde{\epsilon}_a$. Conceptually viewing chemical bonding as consecutive steps in Fig. 1, the renormalized
 239 adsorbate state then couples with the narrowly distributed d -states, shifting up in energies due to orbital
 240 orthogonalization that increases the kinetic energy of electrons and splitting into bonding and anti-bonding
 241 states. One important information from this framework is the evolving density of states projected onto the
 242 adsorbate orbital $|a\rangle$ upon adsorption

$$\rho_a(\epsilon) = \frac{1}{\pi} \frac{\Delta(\epsilon)}{[\epsilon - (\epsilon_a + \Lambda(\epsilon))]^2 + \Delta(\epsilon)^2}, \quad (2)$$

243 in which spin is neglected for simplicity. The effective adsorbate energy level, denoted by ϵ_a , is determined
 244 by the image potential of a charged particle in front of conducting surfaces and the Coulomb repulsion
 245 between electrons in the same orbital [14]. The chemisorption function $\Delta(\epsilon)$ includes contributions from

246 the *sp*-states and the *d*-states

$$\Delta(\epsilon) = \pi \sum_k V_{ak}^2 \delta(\epsilon - \epsilon_k) = \Delta_{sp} + \Delta_d. \quad (3)$$

To simplify the matter, only the 2nd step interaction, i.e., the coupling of the renormalized adsorbate state with the substrate *d*-states, is explicitly considered in Eq. 2. As a new development in our approach, we include an energy-independent constant Δ_{sp}^0 along with Δ_d as the chemisorption function $\Delta(\epsilon)$. The inclusion of Δ_{sp}^0 provides a lifetime broadening of the adsorbate state, serving as a mathematical trick to avoid burdensome sampling of the resonance, i.e., the Lorentzian distribution $\tilde{\rho}_a$ from the 1st step interaction in Fig. 1. Accordingly, ϵ_a will be replaced by the renormalized adsorbate state at $\tilde{\epsilon}_a$. Attributed to the narrowness of a typical metal *d*-band, Δ_d can be simplified as the projected density of *d*-states onto the metal site $\rho_d(\epsilon)$ modulated by an effective coupling integral squared V_{ad}^2 , i.e., $\Delta_d \simeq \pi V_{ad}^2 \rho_d(\epsilon)$. $\Lambda(\epsilon)$ is the Hilbert transform of $\Delta(\epsilon)$. In this framework, the interaction energy between the adsorbate and the substrate can be partitioned into two contributions, i.e., ΔE_{sp} and ΔE_d . ΔE_{sp} is the energy change due to the interaction of the unperturbed adsorbate orbital(s) with the delocalized *sp*-states, while ΔE_d is the energy contribution from further interactions with the localized *d*-states of the substrate. Since all *d*-block metals have a similar, free-electron-like *sp*-band, ΔE_{sp} can be approximated as a surface-independent constant ΔE_{sp}^0 albeit the largest contribution to bonding [17]. To calculate ΔE_d , we include both the attractive orbital hybridization ΔE_d^{hyb} and repulsive orbital orthogonalization ΔE_d^{orth} [27, 38]:

$$\begin{aligned} \Delta E_d^{hyb} &= \frac{2}{\pi} \int_{-\infty}^{\epsilon_F} \tan^{-1} \left(\frac{\Delta(\epsilon)}{\epsilon - \tilde{\epsilon}_a - \Lambda(\epsilon)} \right) d\epsilon - 2 \int_{-\infty}^{\epsilon_F} \epsilon \tilde{\rho}_a d\epsilon \\ \Delta E_d^{orth} &= 2(\langle \tilde{n}_a \rangle + f) S_{ad} |V_{ad}|. \end{aligned} \quad (4)$$

247 The constant 2 considers spin degeneracy of the orbital, $\langle \tilde{n}_a \rangle$ is the occupancy of the renormalized adsorbate
 248 state by integrating the Lorentzian distribution $\tilde{\rho}_a$ up to the Fermi level ϵ_F (taken as 0), and f is the idealized
 249 *d*-band filling of the metal atom. The \tan^{-1} is defined to lie between $-\pi$ to 0 since Δ_{sp}^0 is a non-zero
 250 constant across the energy scale [-15, 15] eV. Thus there is no need to explicitly include localized states
 251 even if present below or above the *d*-band. As a good approximation, the overlap integral S_{ad} is linearly
 252 proportional to the coupling integral for a given adsorbate, i.e., $S_{ad} \approx \alpha |V_{ad}|$, in which α is termed the
 253 orbital overlap coefficient. Similarly, the effective coupling integral squared V_{ad}^2 can be written as $\beta \bar{V}_{ad}^2$,
 254 where β denotes the orbital coupling coefficient and \bar{V}_{ad}^2 characterizes the interorbital coupling strength
 255 when the bonding atoms are aligned along the *z*-axis at a given distance [39]. Its values of *d*-block metals
 256 relative to that of Cu are readily available on the Solid State Table [19].

257 **Bayesian learning** Due to the computationally intensive nature of the MCMC algorithm, there is a need for
 258 a more efficient implementation of the Newns-Anderson-Grimley model than what is obtained by Python
 259 and standard libraries like SciPy and NumPy. We make extensive use of Cython, a C++ extension to the
 260 standard Python, to speed up the performance (10–1000 times) of some CPU-intensive functions in the
 261 model, e.g., Hilbert transform. To perform MCMC sampling, we use PyMC, a flexible and extensible
 262 Python package which includes a wide selection of built-in statistical distributions and sampling algorithms
 263 [40], e.g., Metropolis-Hastings. A “burn-in” of the first half of the samplings and then thinning (1 out of
 264 5 samplings) was performed to ensure that subsequent ones are representative of the posterior distribution.
 265 Convergence of our MCMC-based sampling was verified using parallel chains [25]. The MCMC sampling
 266 results can be directly visualized using *corner*, a open-source Python module. We took Normal for floating-
 267 point variables unrestricted in sign, LogNormal for non-negative parameters, and Uniform for others. ΔE_{sp}^0
 268 and $\tilde{\epsilon}_a$ can be estimated from DFT calculations of the adsorbate on a simple metal, e.g., sodium (Na) at the
 269 face-centered cubic (fcc) phase. Specifically, for *O, we used $\Delta E_{sp}^0 \sim N(-5.0, 1)$, $\tilde{\epsilon}_a \sim N(-5, 1)$, $\Delta_{sp}^0 \sim$
 270 $LN(1, 0.25)$, $\beta \sim LN(2, 1)$, and $\alpha \sim U(0, 1)$. For *OH, we used $\Delta E_{sp}^0 \sim N(-3.0, 1)$, $\tilde{\epsilon}_a^{3\sigma} \sim N(-6, 1)$,
 271 $\tilde{\epsilon}_a^{1\pi} \sim N(-2, 1)$, and $\tilde{\epsilon}_a^{4\sigma^*} \sim N(4, 1)$. We assume that the predicted adsorption properties from Eqs. 2 and
 272 4 are subject to independent normal errors. Specifically, for the property Y and the surface i we have

$$Y_i = \hat{Y}_i(\vec{\theta}) + \sigma \epsilon_i, \quad i = 1, 2, \dots, n \quad (5)$$

273 where ϵ_i is an independent and standard normal random variable and σ is the standard deviation, allowing
 274 for a mismatch between the model prediction $\hat{Y}_i(\vec{\theta})$ and the DFT ground truth Y_i . In this approach, we
 275 define the likelihood function of the property Y from n observations [41]

$$P(Y|\vec{\theta}, \sigma) \propto \sigma^{-n} \exp \left[-\frac{1}{2\sigma^2} \sum_{i=1}^n \left\{ Y_i - \hat{Y}_i(\vec{\theta}) \right\}^2 \right], \quad (6)$$

276 where the sum runs over n training samples for the property Y , which is either the projected density of
 277 states onto an adsorbate orbital or adsorption energies. For adsorption energies, Y_i and \hat{Y}_i are scalar values
 278 with no ambiguity. For projected density of states, it is a vector of paired values, i.e., the one-electron
 279 energy of a state and its probability density, thus deserving a clarification. The mean squared residuals of
 280 model prediction from Eq. 2 for the surface i is used as $\{Y_i - \hat{Y}_i(\vec{\theta})\}^2$ in Eq. 6. To compute the transition
 281 probability of each MCMC step, we define the sum of the (negative) logarithm of the likelihood functions
 282 corresponding to projected density of states onto each adsorbate orbital and binding energies with a hyper-
 283 parameter λ adjusting the weight of two contributing metrics, i.e., $-\sum \ln(P_{\rho_a}) - \lambda \ln(P_{\Delta E})$. To optimize
 284 this parameter, we varied it on a grid of 1, 10, 100, and 1000, and found that 100 is the optimal value to

285 obtain the best performance in adsorption energy prediction. The complete code of Bayesian inference is
286 available at a Github repository <https://github.com/hlxin/bayeschem> for public access.

- 287 [1] A. Nilsson, L. Pettersson, and J. K. Nørskov, *Chemical bonding at surfaces and interfaces* (Elsevier,
288 Amsterdam; Oxford, 2008).
- 289 [2] G. A. Somorjai and Y. Li, *Introduction to Surface Chemistry and Catalysis* (John Wiley & Sons, 2010).
- 290 [3] F. Calle-Vallejo, N. G. Inoglu, H.-Y. Su, J. I. Martínez, I. C. Man, M. T. M. Koper, J. R. Kitchin, and
291 J. Rossmeisl, *Chem. Sci.* **4**, 1245 (2013).
- 292 [4] Y. Y. Tong, A. J. Renouprez, G. A. Martin, and J. J. van der Klink, in *Studies in Surface Science
293 and Catalysis*, Vol. 101, edited by J. W. Hightower, W. Nicholas Delgass, E. Iglesia, and A. T. Bell
294 (Elsevier, 1996) pp. 901–910.
- 295 [5] B. Hammer and J. K. Nørskov, *Surf. Sci.* **343**, 211 (1995).
- 296 [6] A. Vojvodic, J. K. Nørskov, and F. Abild-Pedersen, *Top. Catal.* **57**, 25 (2014).
- 297 [7] H. Xin, A. Vojvodic, J. Voss, J. K. Nørskov, and F. Abild-Pedersen, *Phys. Rev. B Condens. Matter* **89**,
298 115114 (2014).
- 299 [8] X. Ma, Z. Li, L. E. K. Achenie, and H. Xin, *J. Phys. Chem. Lett.* **6**, 3528 (2015).
- 300 [9] Z. Li, S. Wang, W. S. Chin, L. E. Achenie, and H. Xin, *J. Mater. Chem. A Mater. Energy Sustain.* **5**,
301 24131 (2017).
- 302 [10] K. Tran and Z. W. Ulissi, *Nature Catalysis* **1**, 696 (2018).
- 303 [11] A. Palizhati, W. Zhong, K. Tran, S. Back, and Z. W. Ulissi, *J. Chem. Inf. Model.* (2019).
- 304 [12] M. Andersen, S. V. Levchenko, M. Scheffler, and K. Reuter, *ACS Catal.* **9**, 2752 (2019).
- 305 [13] P. W. Anderson, *Phys. Rev.* **124**, 41 (1961).
- 306 [14] D. M. Edwards and D. M. Newns, *Phys. Lett. A* **24**, 236 (1967).
- 307 [15] T. B. Grimley, *Proc. Phys. Soc. London* **90**, 751 (1967).
- 308 [16] T. Bayes and N. Price, *Philosophical Transactions of the Royal Society of London* **53**, 370 (1763).
- 309 [17] B. Hammer, Y. Morikawa, and J. K. Nørskov, *Phys. Rev. Lett.* **76**, 2141 (1996).
- 310 [18] See Supplemental Material at <http://link.aps.org/supplemental/10.1103/PhysRevLett.>, which includes
311 Refs. , for computational details and discussion..
- 312 [19] W. A. Harrison and Physics, *Electronic Structure and the Properties of Solids: The Physics of the
313 Chemical Bond* (Dover Publications, New York, 1989).

- 314 [20] E. Santos, P. Quaino, and W. Schmickler, *Phys. Chem. Chem. Phys.* **14**, 11224 (2012).
- 315 [21] A. M. Román, J. Dudoff, A. Baz, and A. Holewinski, *ACS Catal.* **7**, 8641 (2017).
- 316 [22] D. S. Mebane, K. Sham Bhat, J. D. Kress, D. J. Fauth, M. L. Gray, A. Lee, and D. C. Miller, *Phys.*
317 *Chem. Chem. Phys.* **15**, 4355 (2013).
- 318 [23] J. Wellendorff, K. T. Lundgaard, A. Møgelhøj, V. Petzold, D. D. Landis, J. K. Nørskov, T. Bligaard,
319 and K. W. Jacobsen, *Phys. Rev. B Condens. Matter* **85**, 235149 (2012).
- 320 [24] E. A. Walker, D. Mitchell, G. A. Terejanu, and A. Heyden, *ACS Catal.* **8**, 3990 (2018).
- 321 [25] D. Gamerman and H. F. Lopes, *Markov Chain Monte Carlo: Stochastic Simulation for Bayesian*
322 *Inference, Second Edition (Chapman & Hall/CRC Texts in Statistical Science)*, 2nd ed. (Chapman and
323 Hall/CRC, 2006).
- 324 [26] B. Hammer and J. K. Nørskov, in *Chemisorption and Reactivity on Supported Clusters and Thin*
325 *Films: Towards an Understanding of Microscopic Processes in Catalysis*, edited by R. M. Lambert
326 and G. Pacchioni (Springer Netherlands, Dordrecht, 1997) pp. 285–351.
- 327 [27] B. Hammer and J. K. Nørskov, in *Chemisorption and Reactivity on Supported Clusters and Thin*
328 *Films: Towards an Understanding of Microscopic Processes in Catalysis*, edited by R. M. Lambert
329 and G. Pacchioni (Springer Netherlands, Dordrecht, 1997) pp. 285–351.
- 330 [28] K. Wandelt, *Surf. Sci. Rep.* **2**, 1 (1982).
- 331 [29] H. Xin and S. Linic, *J. Chem. Phys.* **132**, 221101 (2010).
- 332 [30] H. Xin, A. Holewinski, and S. Linic, *ACS Catal.* **2**, 12 (2012).
- 333 [31] M. T. Tang, H. Peng, P. S. Lamoureux, M. Bajdich, and F. Abild-Pedersen, “From electricity to fuels:
334 Descriptors for C₁ selectivity in electrochemical CO₂ reduction,” (2019).
- 335 [32] D. Strmcnik, M. Uchimura, C. Wang, R. Subbaraman, N. Danilovic, D. v. d. Vliet, A. P. Paulikas,
336 V. R. Stamenkovic, and N. M. Markovic, *Nat. Chem.* **5**, 300 (2013).
- 337 [33] Z. Li, X. Ma, and H. Xin, *Catal. Today* **280, Part 2**, 232 (2017).
- 338 [34] H. Thirumalai and J. R. Kitchin, *Top. Catal.* (2018).
- 339 [35] M. T. Greiner, T. E. Jones, S. Beeg, L. Zwiener, M. Scherzer, F. Girgsdies, S. Piccinin, M. Armbrüster,
340 A. Knop-Gericke, and R. Schlögl, *Nat. Chem.* (2018).
- 341 [36] P. Giannozzi, S. Baroni, N. Bonini, M. Calandra, R. Car, C. Cavazzoni, D. Ceresoli, G. L. Chiarotti,
342 M. Cococcioni, I. Dabo, A. Dal Corso, S. de Gironcoli, S. Fabris, G. Fratesi, R. Gebauer, U. Ger-
343 stmann, C. Gouguassis, A. Kokalj, M. Lazzeri, L. Martin-Samos, N. Marzari, F. Mauri, R. Maz-
344 zarello, S. Paolini, A. Pasquarello, L. Paulatto, C. Sbraccia, S. Scandolo, G. Sclauzero, A. P. Seitsonen,

- 345 A. Smogunov, P. Umari, and R. M. Wentzcovitch, J. Phys. Condens. Matter **21**, 395502 (2009).
- 346 [37] J. P. Perdew, K. Burke, and M. Ernzerhof, Phys. Rev. Lett. **77**, 3865 (1996).
- 347 [38] A. Vojvodic, J. K. Nørskov, and F. Abild-Pedersen, Top. Catal. **57**, 25 (2014).
- 348 [39] X. Ma and H. Xin, Phys. Rev. Lett. **118**, 036101 (2017).
- 349 [40] A. Patil, D. Huard, and C. J. Fonnesbeck, J. Stat. Softw. **35**, 1 (2010).
- 350 [41] A. W. Baggaley, G. R. Sarson, A. Shukurov, R. J. Boys, and A. Golightly, Phys. Rev. E Stat. Nonlin.
- 351 Soft Matter Phys. **86**, 016105 (2012).

352 **Acknowledgements**

353 **Acknowledgments**

354 S.W., H.S.P., N.O., and H.X. acknowledge the financial support from the NSF CAREER program

355 (CBET-1845531). The computational resource used in this work is provided by the advanced research

356 computing at Virginia Polytechnic Institute and State University.

Figures

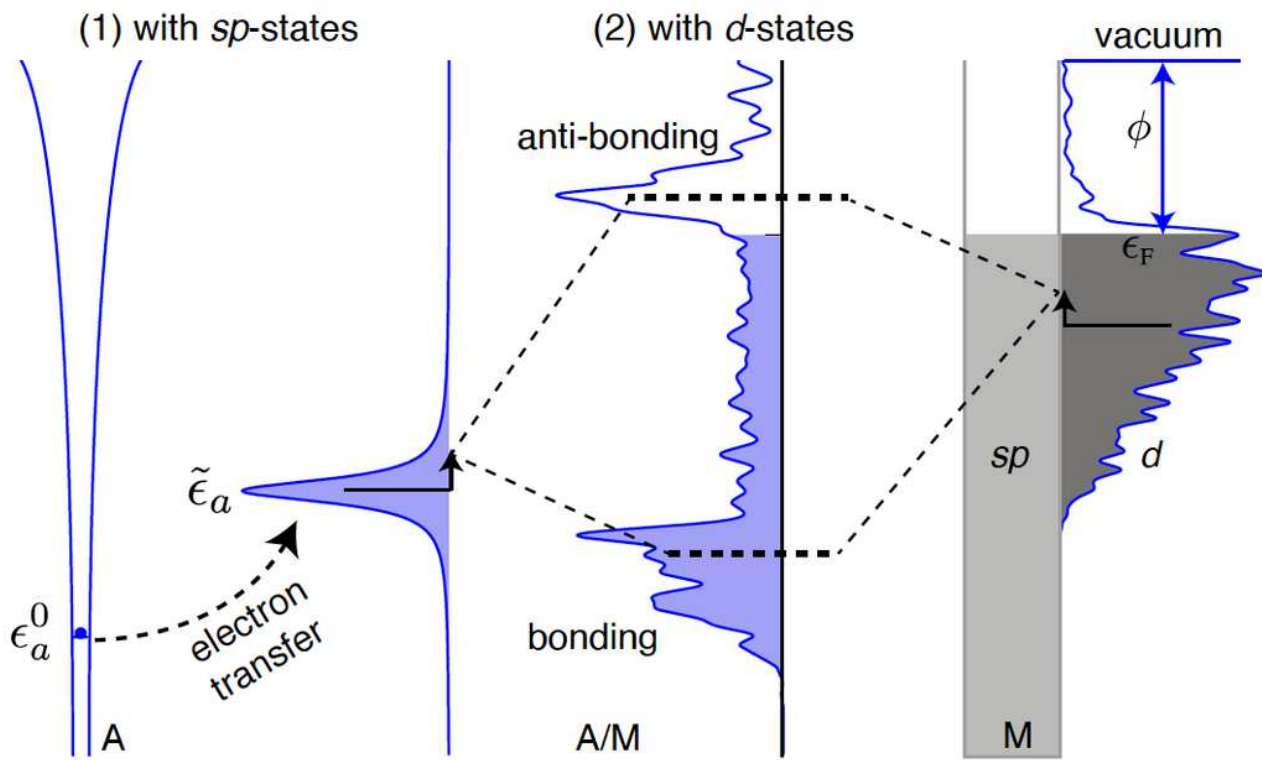


Figure 1

Illustration of chemical bonding at transition-metal surfaces within the d-band reactivity theory. An adsorbate A with a valence electron at a discrete energy level ϵ_a^0 first interacts with the free-electronlike sp-states of the substrate M, forming a broadened resonance at $\sim \epsilon_a$ accompanied with electron transfer. Conceptually, it further overlaps and hybridizes with the narrowly distributed d-states, which leads to a splitting into bonding and anti-bonding states. The work function ϕ and Fermi level ϵ_F of M are marked.

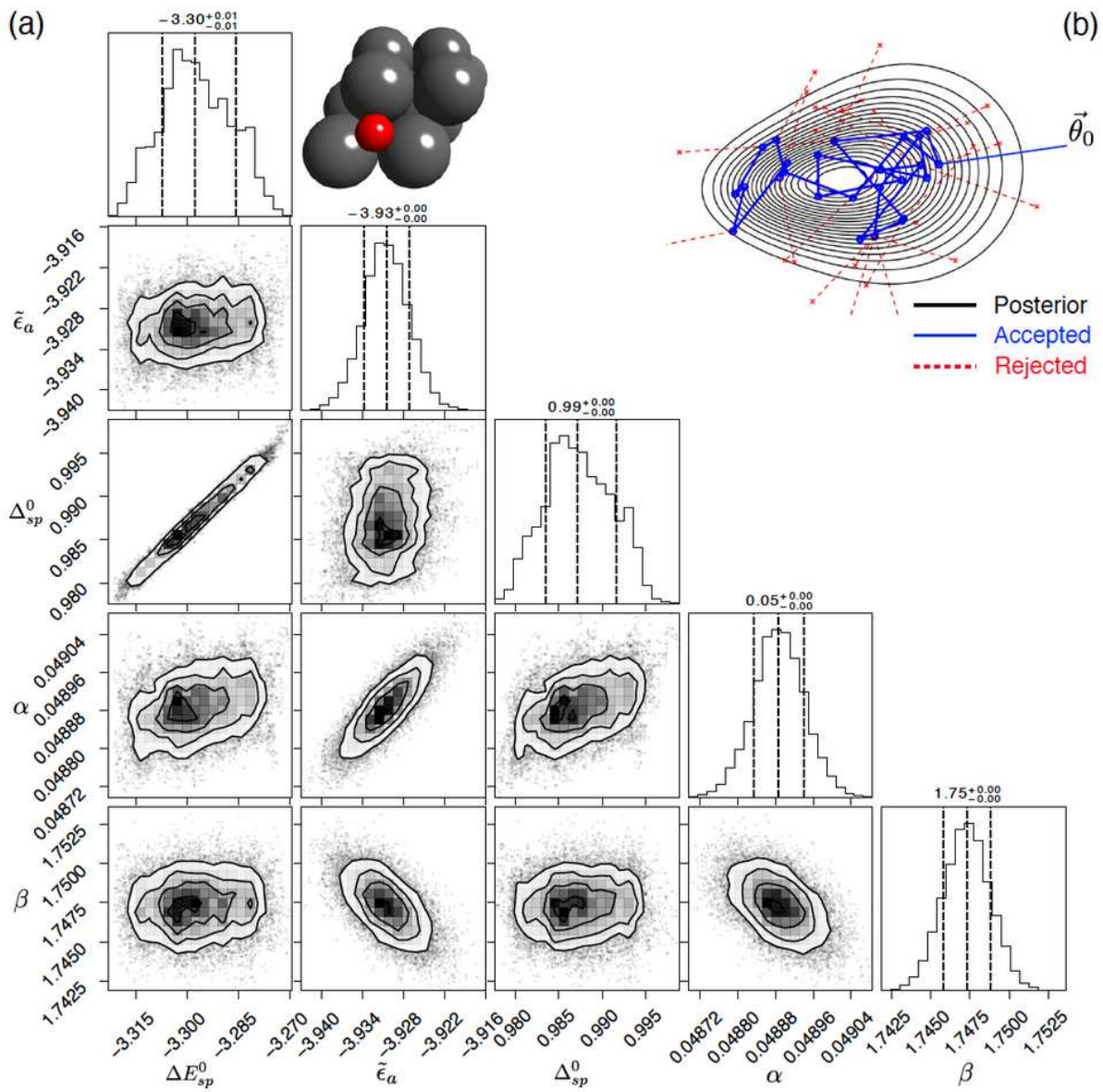


Figure 2

Bayesian parameterization. a The co-variance of the joint posterior distribution for each parameter pair and the 1D histogram of model parameters (ΔE_{sp}^0 , $\tilde{\epsilon}_a$, $\Delta_0^0_{sp}$, α , and β) from MCMC simulations for *O adsorption at the fcc-hollow site of the {111}-terminated transition-metal surfaces. A top view of the model structure is shown in inset. b Schematic illustration of the MCMC sampling in a multi-dimensional parameter space.

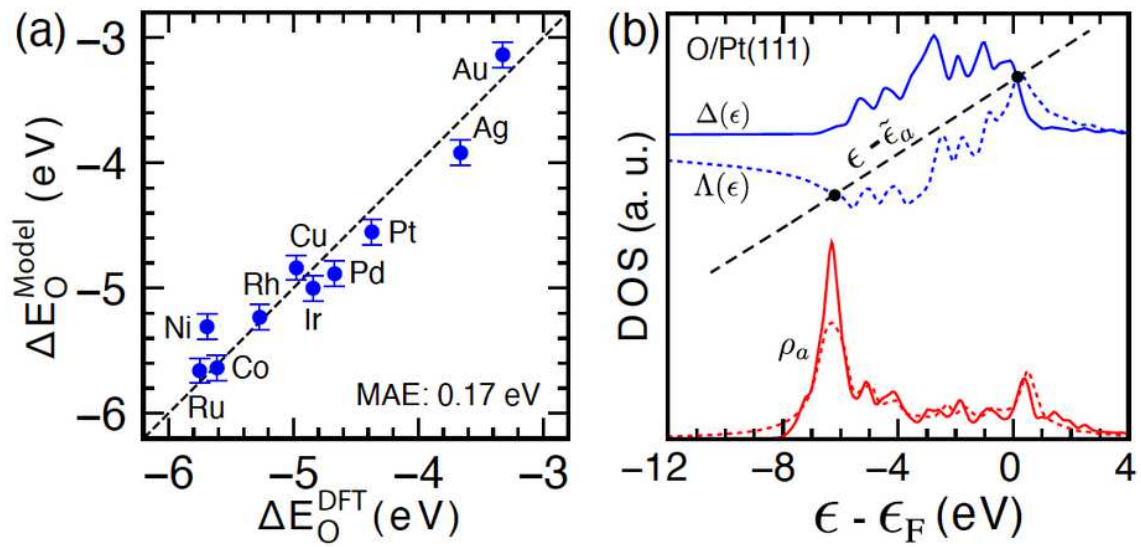


Figure 3

Model-predicted adsorption properties. a DFT-calculated *O adsorption energies (atomic O as the reference) at transition-metal surfaces vs. model prediction using the posterior distribution of model parameters (θ ; σ). Error bars represent the standard deviation of model prediction with 1000 random draws from converged trajectories. b Projected density of states onto the O_{2p} orbital from DFT calculations (solid) and model prediction (dashed) using the posterior means of model parameters, taking Pt(111) as an example. The graphical solution to the Newns-Anderson-Grimley model is also shown, in which the adsorbate-substrate bonding and anti-bonding states are clearly captured.

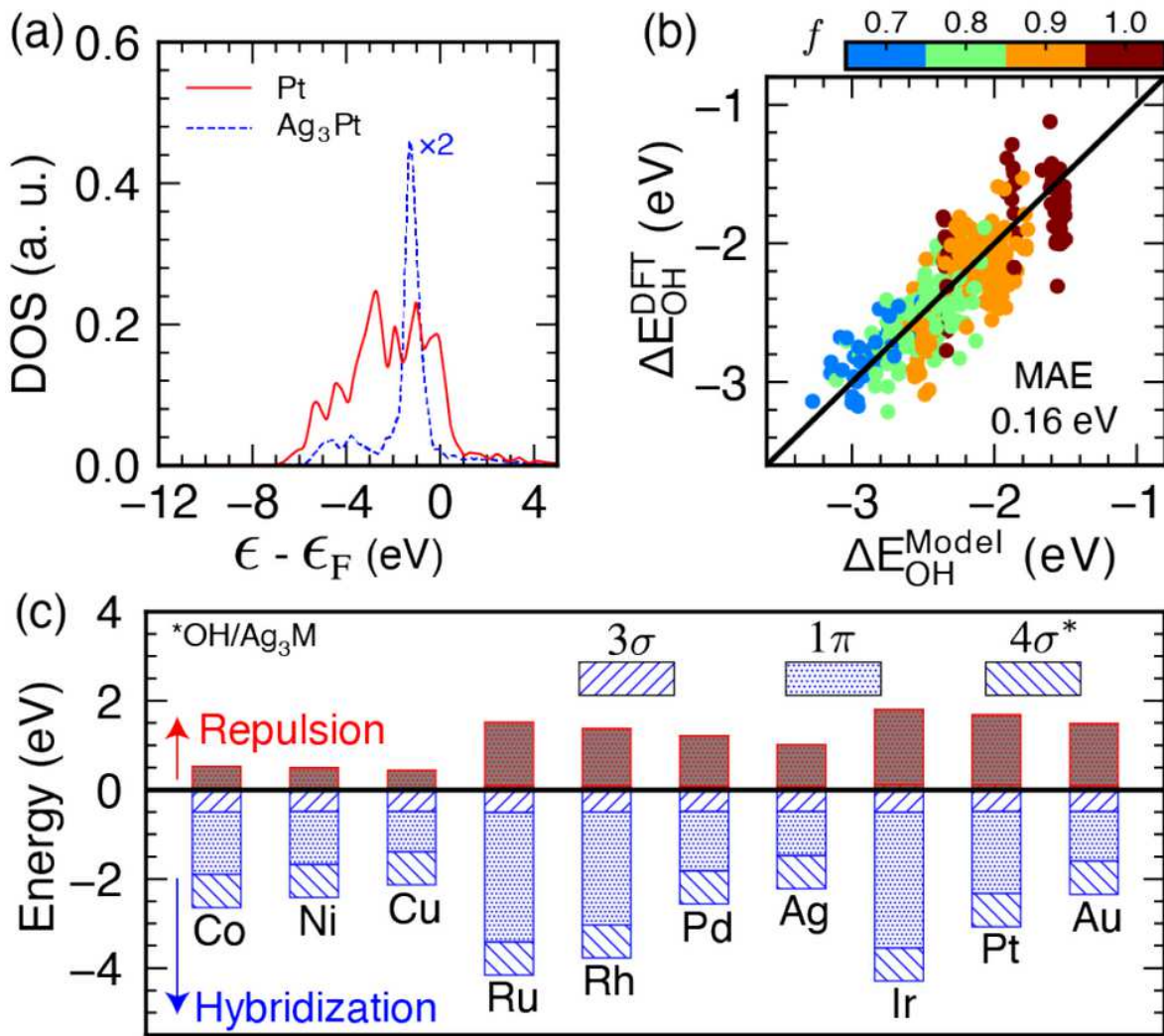


Figure 4

Model test and interpretation. a The d-states of a transition-metal site exhibit diverse characteristics ranging from bulk-like semi-elliptic bands to free-atom-like discrete energy levels (Pt and Ag_3Pt as examples). b DFT-calculated vs. model-predicted adsorption energies of ${}^*\text{OH}$ at the atop site of {111}-terminated intermetallics and near-surface alloys. c Partition of ${}^*\text{OH}$ adsorption energies at the M site of Ag_3M into orbital hybridization and orthogonalization of 3σ , 1π , and $4\sigma^*$ orbitals with the metal d-states.

Supplementary Files

This is a list of supplementary files associated with this preprint. Click to download.

- supp.pdf